IOP Publishing | International Atomic Energy Agency Nuclear Fusion

Nucl. Fusion **57** (2017) 016005 (7pp) doi:10.1088/0029-5515/57/1/016005

Effect of resonant magnetic perturbations on microturbulence in DIII-D pedestal

I. Holod[1,2], Z. Lin[1], S. Taimourzadeh[1], R. Nazikian[3], D. Spong[4] and A. Wingen[4]

[1] Department of Physics and Astronomy, University of California, Irvine, CA 92697, USA
[2] Lawrence Livermore National Laboratory, Livermore, CA 94550, USA
[3] Princeton Plasma Physics Laboratory, Princeton, NJ 08543, USA
[4] Oak Ridge National Laboratory, Oak Ridge, TN 37831, USA

E-mail: iholod@uci.edu

Received 14 July 2016, revised 7 September 2016
Accepted for publication 12 September 2016
Published 3 October 2016

Abstract

Vacuum resonant magnetic perturbations (RMP) applied to otherwise axisymmetric tokamak plasmas produce in general a combination of non-resonant effects that preserve closed flux surfaces (kink response) and resonant effects that introduce magnetic islands and/or stochasticity (tearing response). The effect of the plasma kink response on the linear stability and nonlinear transport of edge turbulence is studied using the gyrokinetic toroidal code GTC for a DIII-D plasma with applied $n = 2$ vacuum RMP. GTC simulations use the 3D equilibrium of DIII-D discharge 158103 (Nazikian *et al* 2015 *Phys. Rev. Lett.* **114** 105002), which is provided by nonlinear ideal MHD VMEC equilibrium solver in order to include the effect of the plasma kink response to the external field but to exclude island formation at rational surfaces. Analysis using the GTC simulation results reveal no increase of growth rates for the electrostatic drift wave instability and for the electromagnetic kinetic-ballooning mode in the presence of the plasma kink response to the RMP. Furthermore, nonlinear electrostatic simulations show that the effect of the 3D equilibrium on zonal flow damping is very weak and found to be insufficient to modify turbulent transport in the electrostatic turbulence.

Keywords: tokamak, turbulence, plasma, resonant magnetic perturbation, edge localized mode

(Some figures may appear in colour only in the online journal)

1. Introduction

Stability and confinement of tokamak H-mode operation depend crucially on properties of the plasma pedestal—the outer region of the plasmas characterized by steep pressure gradients and enhanced edge currents. Due to these large gradients and enhanced edge current, the pedestal is subject to dangerous magneto-hydrodynamic instabilities, referred to as edge localized modes (ELMs). These instabilities cause a partial collapse of the pedestal profiles, and induce significant heat and particle fluxes to material surfaces, which may lead to significant erosion of plasma facing materials on reactor-scale devices. One possibility to mitigate or eliminate ELMs is to apply resonant magnetic perturbations (RMP) [1], which cause significant changes in the edge transport [2–4]. Fast transport bifurcations in and out of ELM suppression with static RMPs [3] and fast RMP modulation experiments [4] show that the response of the turbulence to the applied RMP is faster than the profile evolution time, suggesting a possible direct effect of the RMP modified 3D equilibrium on the edge turbulence. The effect of the RMP on the plasma equilibrium can be represented by a non-resonant part (ideal MHD kink response) and a resonant part (island formation at rational surfaces). A key question is whether the ideal MHD modification of the axisymmetric equilibrium by non-axisymmetric vacuum RMPs fields can modify the linear growth rates of high-n electrostatic or electromagnetic low-n instabilities, or modify the damping of zonal flows sufficiently to drive profile change observed in the transition from ELM mitigated to ELM suppressed conditions. If ideal MHD effects are insufficient to change the linear growth rates of the drift-Alfvénic instabilities or of zonal flows, then other physics must account

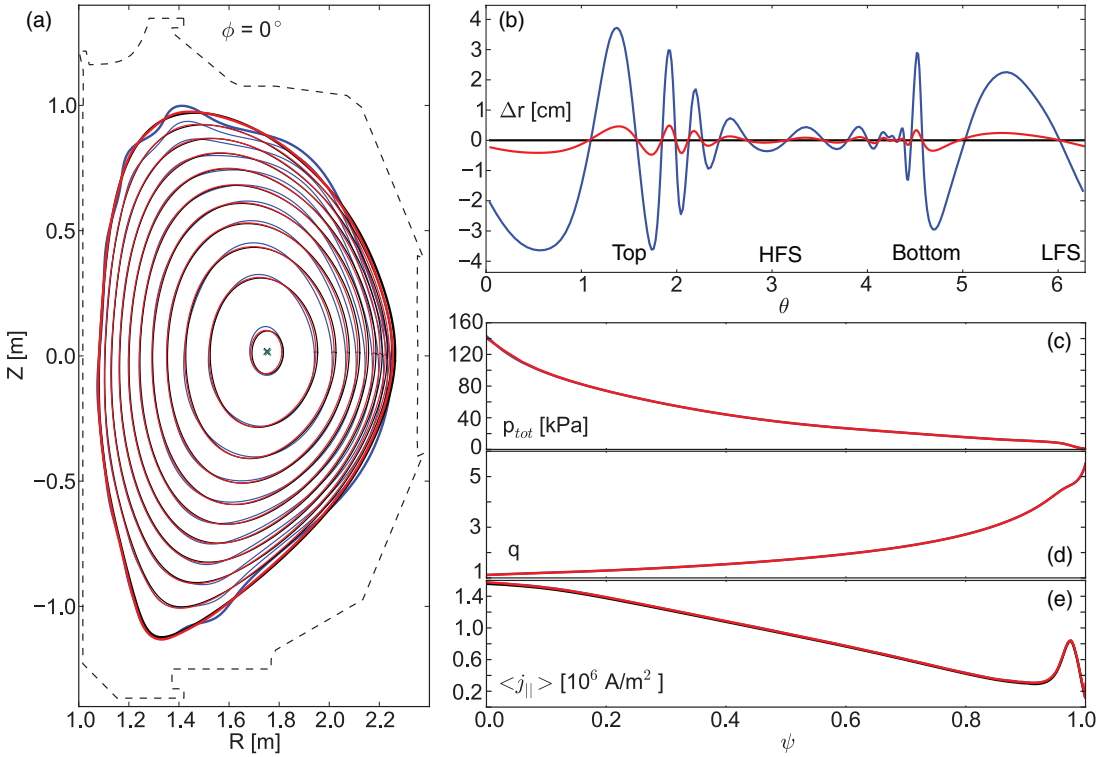

Figure 1. VMEC equilibria for 158103 at 3050 ms: axisymmetric (black), RMP (red), RMP × 10 (blue). (*a*) Cross-section at toroidal angle 0. (*b*) Deviation of the RMP boundary from the axisymmetry boundary. (*c*) Pressure profile. (*d*) Safety factor. (*e*) Parallel current density.

for the observed transport change. This additional physics may be related to the neoclassical response to 3D fields or to non-ideal MHD effects of the plasma such as tearing modes. The purpose of this paper is to establish that the ideal MHD response to the RMP is insufficient to affect fluctuation induced transport and thus we are drawn to the conclusion that other physics must come into play for affecting profile and fluctuation changes in the pedestal.

In principle, changes in transport in the tokamak edge that lead to ELM suppression by RMPs or by edge harmonic oscillations (EHO) [5] could arise from the effect of the ideal MHD kink response on the turbulent and neoclassical transport. The effects of the 3D magnetic fields due to the plasma kink response have been studied theoretically in several publications. Using a local 3D equilibrium model, the 3D modulation of the local magnetic shear was found to modify the infinite-n ideal MHD ballooning stability boundary in the $s-\alpha$ parameter space [6]. The enhancement of the high-n ballooning mode instability by $n=3$ RMP was also reported in ideal MHD COBRA simulations using local geometry in radial and toroidal angle space [7]. The enhanced zonal flow damping by 3D magnetic fields has been shown in the resistive drift wave turbulence using an extended Hasegawa–Wakatani fluid model [8]. A magnetic-flutter-induced electron transport model was invoked to drive the enhanced electron transport by RMP and to induce an ambipolar radial electric field [9]. The effects of stochastic magnetic fields have also been studied. A radial plasma flow due to the electric field modified by the electron stochastic loss was invoked to model the pump-out effect [10]. Similarly, a quasilinear transport model was constructed to explain the RMP density pump-out in DIII-D [11].

RMP mitigation of ELMs likely involves multiple physical processes and their complicated interplay. Numerical simulation provides a powerful tool allowing separation and investigation of key mechanisms using an incremental approach. In this work we address specifically the effect of the 3D equilibrium due to the ideal MHD response of the plasma to an applied vacuum RMP in a typical DIII-D H-mode discharge. Other nonideal MHD effects such as island formation and stochasticity are left for the future work. For the purpose of this paper, the same density and temperature profiles are used in all simulations based on the experimental inhomogeneity scale length in the middle of the pedestal in DIII-D shot 158103 at 3050 ms, corresponding to a typical ITER similar shape (ISS) discharge with ELM suppression reported in [3, 12] with an applied $n=2$ RMP. This means that we do not address the effect of profile change on stability. Rather we address whether such profile changes can be induced by a change of stability arising from the changes in the 3D magnetic equilibrium. For the same reason and for simplicity, the radial electric field, equilibrium flows and collisions are excluded from these simulations presented in this paper and will be addressed in a future work.

The set of magnetic equilibria is modeled by the VMEC code [13], which retains closed flux surface topology. Three cases are considered: the equilibrium with applied $n=2$ RMP of experimental magnitude with a vacuum $\delta B/B \sim 5\times10^{-4}$ at the plasma edge; the corresponding axisymmetric equilibrium (with no RMP), and the equilibrium with RMP amplitude amplified by a factor of 10. Our previous studies in axisymmetric equilibria recover the kinetic ballooning mode (KBM) and show it to be marginally unstable for typical DIII-D

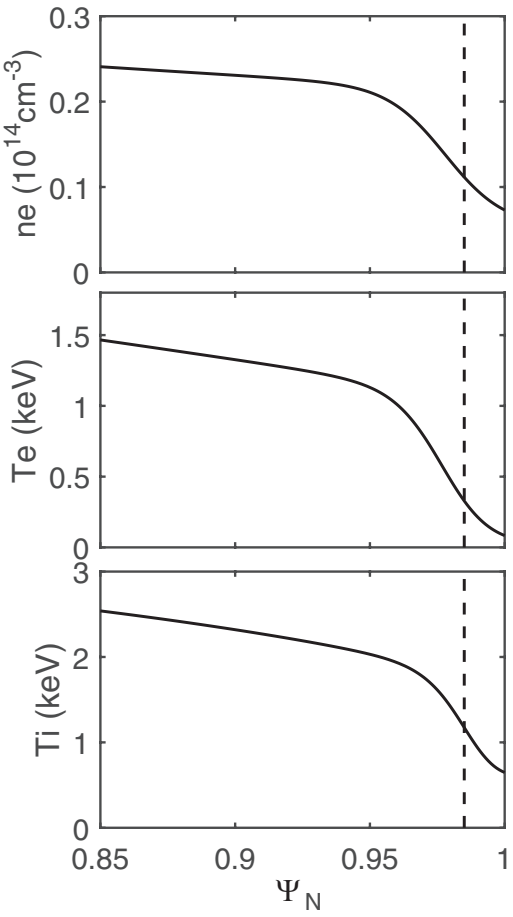

Figure 2. Equilibrium density and temperature profiles of the DIII-D pedestal (shot 158103 at 3050 ms). Vertical dashed line indicates the $\psi_N = 0.985$ location.

Table 1. Electrostatic GTC simulation results of DIII-D shot 158103.3050.

	Axi-symmetric	RMP	RMP×10
γ (kHz), ±5kHz	208	208	225
χ_i (m^2 s^{-1}), ±0.5 m^2 s^{-1}	3.0	2.9	3.0
χ_e (m^2 s^{-1}), ±0.5 m^2 s^{-1}	2.9	2.8	2.9
Γ (m^2 s^{-1}), ±0.3 m^2 s^{-1}	1.2	1.1	1.1

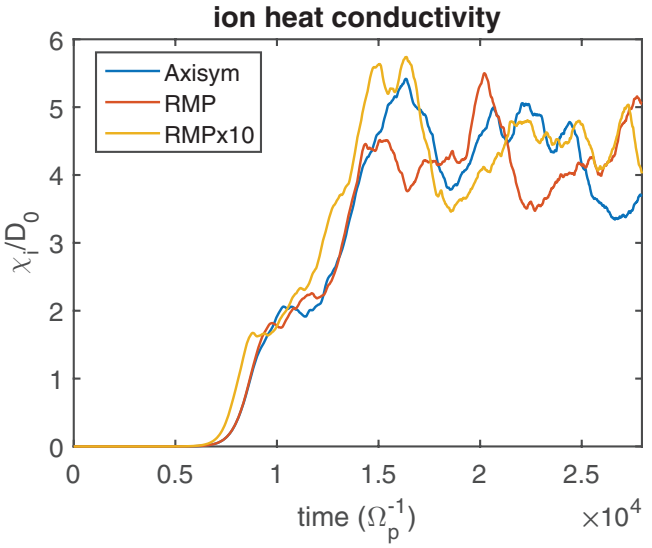

Figure 3. Time evolution of the ion heat conductivity for different equilibria (from GTC electrostatic simulation using local gradients taken at $\psi_N = 0.985$).

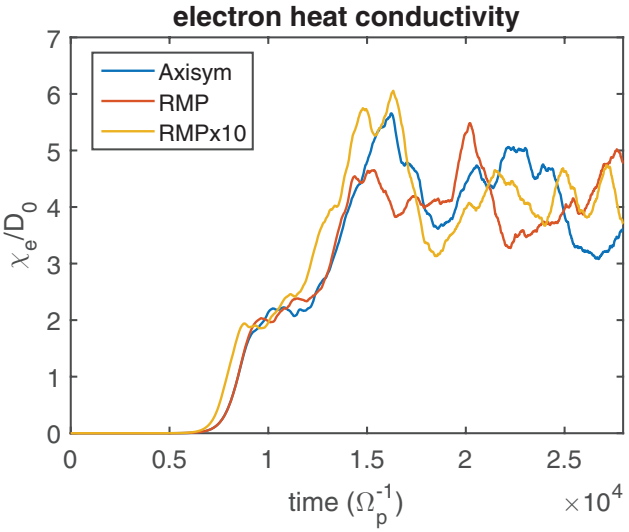

Figure 4. Time evolution of the electron heat conductivity for different equilibria (from GTC electrostatic simulation using local gradients taken at $\psi_N = 0.985$).

pedestal parameters [14]. Thus to investigate the effect of RMP on the KBM, we enhance the KBM instability drive by artificially increasing the electron density in the simulations.

In this work we apply the global gyrokinetic toroidal code GTC [15] to simulate turbulence in the edge of DIII-D tokamak plasmas. The strong variation of plasma parameters in the pedestal region requires using a non-local model. The validity of the so-called local approximation rely on the assumption that $k_\perp L_p \gg 1$, where $k_\perp$ is the perpendicular wavenumber, and L_p is the pressure gradient scale length. While the local assumption can be mostly justified at the top of pedestal where $k_\perp L_p \sim 25$, it is not strictly applicable in the steep gradient region, where $k_\perp L_p \sim 5$, assuming $k_\perp \rho_i \approx 1$. The electromagnetic capability in GTC is implemented by using the fluid-kinetic hybrid electron model [17], including equilibrium current [18].

Overall, we find from the gyrokinetic simulations no increase of electrostatic drift-wave and electromagnetic KBM instability by the RMP using experimental parameters and the VMEC equilibria. There is a small increase of growth rate only for artificially amplified RMP strength at 10 times the applied field strength. Furthermore, the effect of RMP on zonal flow damping and turbulent transport is found to be insignificant for the perturbed magnetic field calculated from ideal MHD. Experimentally, large changes are seen in the turbulent fluctuations in the pedestal when the plasma goes into ELM suppression with applied RMPs. Therefore, the simulations presented here demonstrate that the plasma kink response to the RMP cannot account for the observed increase of the turbulence and therefore some other effects are required on top of the plasma kink response, such as island formation, that may have a stronger effect on turbulent transport.

This paper is organized as follows: in section 2 we describe the GTC simulation model, as well as the way equilibrium is calculated using VMEC solver. In section 3 the results of electrostatic gyrokinetic simulations of turbulence and transport are presented. Simulation studies of the effect of RMP on electromagnetic KBM instability are presented in section 4. The conclusions are summarized in section 5.

2. Simulation setup

In the GTC the ions are simulated by integrating the gyrokinetic equation along the gyrocenter trajectories. The electrons are described by the fluid-kinetic hybrid model [16, 17] based on the separation of the electron response into a dominant adiabatic part $\delta f_e^{(a)}$ and non-adiabatic correction δh_e.

$$\delta f_e \equiv \delta f_e^{(a)} + \delta h_e = \frac{e f_0}{T_e}\delta\phi_{\rm eff} + \left.\frac{\partial f_0}{\partial \psi}\right|_{v_\perp} \delta\psi + \delta h_e, \qquad (1)$$

where f_0 is the equilibrium Maxwellian distribution, T_e is the equilibrium electron temperature, ψ and $\delta\psi$ is the equilibrium and perturbed poloidal magnetic flux function, respectively. The effective potential $\delta\phi_{\rm eff}$ determines the parallel electric field as $\delta E_\parallel = -\nabla_\parallel \delta\phi_{\rm eff}$. In the electrostatic simulations the $\delta\psi$ term in (1) vanishes and $\delta\phi_{\rm eff}$ becomes the electrostatic potential $\delta\phi$ obtained by solving the gyrokinetic Poisson's equation. In the electromagnetic case the $\delta\phi_{\rm eff}$ is obtained from the adiabatic relation using perturbed electron density calculated by the electron continuity equation, and $\delta\psi$ is obtained from the Faraday's equation. Finally, the non-adiabatic correction δh_e is obtained by integrating the electron drift-kinetic equation subtracted by the adiabatic equation involving only free streaming terms. The fluid-kinetic hybrid electron model provides excellent numerical efficiency while preserving the important kinetic effects.

GTC employs magnetic Boozer coordinates for particles, and unstructured field-aligned mesh for the field solvers. Realistic magnetic equilibrium and plasma profiles are implemented using the external input files [19]. GTC capability to simulate general toroidal geometry has been recently expanded to include non-axisymmetric configuration. The equilibrium geometry and magnetic field data is provided in the form of Fourier series coefficients A_{cn}, A_{sn} in ζ-expansion: $A(\psi,\theta,\zeta) = \sum_{i=1}^{N} [A_{cn}(\psi,\theta)\cos(n_i\zeta) + A_{sn}(\psi,\theta)\sin(n_i\zeta)]$, where (ψ,θ,ζ) are poloidal flux, poloidal angle, and toroidal angle, respectively, forming the right-handed Boozer coordinate system. The equilibrium data is provided for the magnetic field strength B, and cylindrical coordinates (R,Φ,Z) of points forming magnetic flux surfaces. Additionally, the flux functions representing poloidal $g(\psi)$ and toroidal $I(\psi)$ currents, magnetic safety factor $q(\psi)$, and minor radius $r(\psi)$ defined as a distance from the magnetic axis along the outer midplane, are provided. The data is presented on the uniform (ψ,θ) grid for all $(n_1 \ldots n_N)$ toroidal harmonics. To reduce the computational load and memory usage, the transformation of non-axisymmetric variables into spline function of ζ is chosen for implementation in GTC, with spline coefficients associated with a particular grid point ζ_i being stored by processors with corresponding toroidal rank using message passing interface (MPI) parallelization.

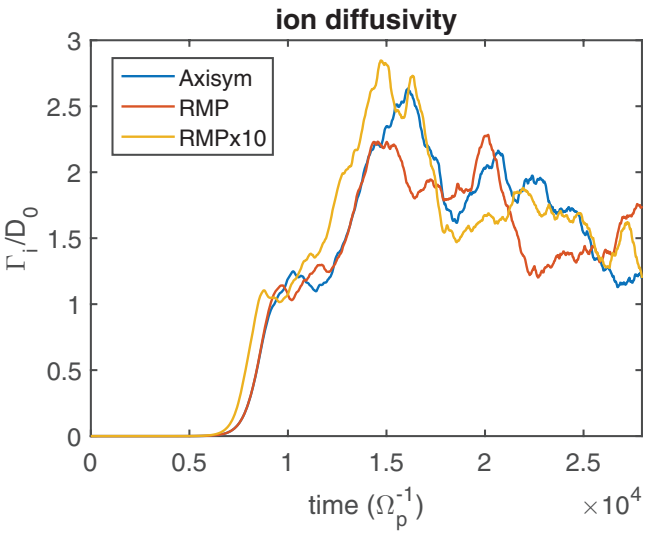

Figure 5. Time evolution of the ion diffusivity for different equilibria (from GTC electrostatic simulation using local gradients taken at $\psi_N = 0.985$).

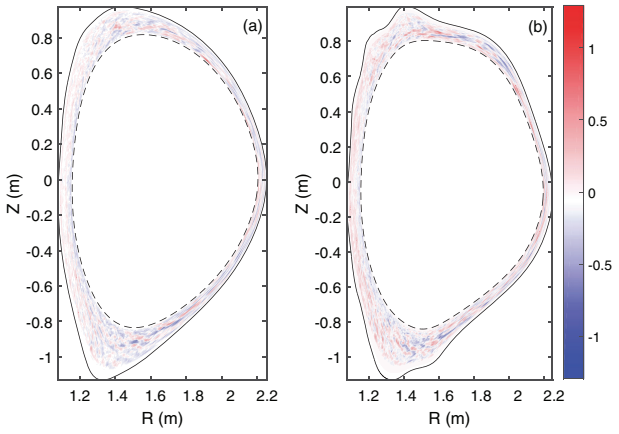

Figure 6. Poloidal snapshot of normalized electrostatic potential $e\phi/T_e$ at the saturated state with RMP (panel (*a*)) and with RMP $\times$ 10 (panel (*b*)) from nonlinear electrostatic GTC simulation. Dashed line indicates the inner boundary of the radial simulation domain.

In all our simulations the convergence in time step, grid size and number of particles is achieved. In this work the typical number of macro-particles per cell for both electron and ion species is $\sim$100, the typical time step is $\Delta t\,\Omega_{ci} \approx 5$. The typical spatial grid resolution is $\Delta r/\rho_i \approx 0.2$, $r\Delta\theta/\rho_i \approx 1$, and 32 grid points in the toroidal directions are required to resolve the parallel field variations. The perturbed potentials are calculated assuming homogeneous Dirichlet radial boundary conditions.

The non-axisymmetric equilibria used for GTC simulations presented in this paper are constructed by the VMEC code [13] in the free boundary mode [20], based on provided axisymmetric kinetic equilibrium and magnetic coils configuration of DIII-D. The axisymmetric kinetic equilibrium is computed by the EFIT code using the measured thermal

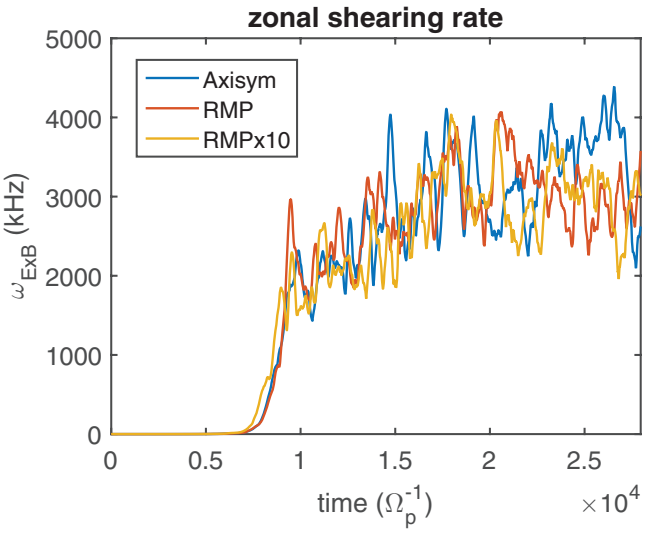

Figure 7. Time evolution of zonal shearing rate magnitude (from GTC electrostatic simulation using local gradients taken at $\psi_N = 0.985$).

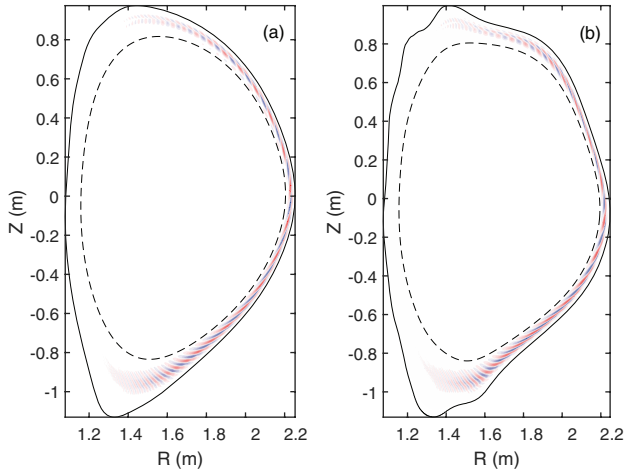

Figure 8. Poloidal snapshot of electrostatic potential from GTC simulation of $n = 20$ KBM with RMP (panel (a)) and RMP×10 (panel (b)). Dashed line indicates the inner boundary of the radial simulation domain.

pressure and computed beam ion pressure and using the Sauter model of the edge bootstrap current as well as the magnetic and internal motional stark effect (MSE) measurements of the magnetic geometry. VMEC, which is a nonlinear, single-fluid, ideal MHD equilibrium code, then solves for force balance, $\nabla P = \mathbf{j} \times \mathbf{B}$, enforcing nested flux surfaces. The resulting equilibrium is a fully 3D equilibrium, including the applied RMP field from the internal coils (I-coils) and its ideal MHD plasma response. The latter means that the kink response is included, while any tearing response (magnetic islands) is not.

VMEC equilibria are computed for three cases: axisymmetric equilibrium, the equilibrium with RMP of experimental amplitude, and the equilibrium with RMP amplitude amplified by a factor of 10. The axisymmetric case does not include 3D fields, while the RMP cases include the $n = 2$ field, applied by the I-coil during the DIII-D experiments. In the RMP × 10 case the currents in the I-coils are magnified by a factor of 10. Figure 1(a) shows the poloidal cross-section for all cases

Table 2. Linear electromagnetic $n = 20$ GTC simulation results of DIII-D shot 158103.3050.

	Axi-symmetric	RMP	RMP × 10
f_r (kHz), ±5 kHz	146	146	146
γ (kHz), ±5 kHz	310	315	334

overlaid. The axisymmetric case in black and the RMP case in red are almost on top of each other. Only the RMP × 10 case in blue makes the 3D structure of the equilibrium clearly visible. The deviation of the VMEC boundary from the axisymmetry boundary is shown in figure 1(b). In the RMP case Δr varies about 1 cm, while in the RMP × 10 case it varies about 7.4 cm. The variation is the largest near the upper and lower X-points of the diverted shape. Figures 1(c)–(e) show the pressure-, q- and current density profiles respectively. The profiles agree in all three cases, so the RMP only changes the structure of the flux surfaces, especially in the edge region.

3. RMP effect on electrostatic microturbulence and transport

In this section we present the results of nonlinear electrostatic gyrokinetic simulations of the DIII-D pedestal under the effect of RMP magnetic perturbation. Due to strongly varying plasma parameters in the pedestal region, it is difficult to identify the dominant local instabilities. In order to do so, in the simulations we use a uniform pressure gradient for the whole radial simulation domain. Similar to our previous studies [14], in this work we construct equilibrium density and temperature profiles using the constant gradient scale length values of $R_0/L_{ne} = 96$, $R_0/L_{Te} = 247$, $R_0/L_{Ti} = 131$ taken from the radial location corresponding to $\psi_N = 0.985$ in the DIII-D shot 158103 at time 3050 ms (figure 2). The smallest equilibrium inhomogeneity scale length is still larger than the ion gyroradius, $\rho_i/L_{Te} \sim 0.2$, ensuring the validity of gyrokinetic ordering [21]. The deuterium ion equilibrium density is set to be equal to the electron density, assuming quasineutrality. Our radial simulation domain ranges from $\psi_N = 0.85$ to $\psi_N = 1.0$, covering the entire pedestal region. While plasma temperature and density profiles are set artificially to drive instabilities from the specific locations inside the pedestal, in GTC simulation we use realistic magnetic geometry modeled by the VMEC code. The inconsistency between plasma pressure profile, used in the simulation, and the magnetic geometry would manifest itself on the profile relaxation time, which is well beyond our time frame of interest.

Electrostatic GTC simulations find strong driftwave turbulence in all three equilibrium cases (axisymmetric, RMP, and RMP ×10). Time evolution of electron and ion heat conductivities and particle diffusivity from the nonlinear GTC simulations using different equilibria are shown in the figures 3–5. Here, the time is normalized by local proton gyrofrequency $\Omega_p = 1.8 \times 10^8\ \mathrm{s}^{-1}$, the heat conductivity and particle diffusivity is normalized by local Gyro-Bohm coefficient $D_0 = (\rho_s/a) k_B T_e/eB \approx 0.7\ \mathrm{m}^2\ \mathrm{s}^{-1}$.

From the initial exponential phase, before nonlinear saturation, we can find the mode linear growth rate, γ. Corresponding values of the growth rate for the different RMP levels are shown in table 1. The largest increase of the growth rate is observed for the RMP $\times$ 10 case, which deviates from the symmetric case by less than 10%.

In the table 1 we also present the time averaged saturated values of ion and electron heat conductivities and particle diffusivity. As we can see, the difference between various equilibria lies within corresponding statistical errors. We emphasize that our simulations are not fully comprehensive, since we ignored collisions and equilibrium flows, thus the values presented in table 1 should only serve for comparison purpose.

The electrostatic turbulent transport is qualitatively determined by the statistical properties of fluctuation spectra and self-generated zonal flows. We have looked at the effect of the ideal MHD response on these two factors.

The electrostatic mode structure in the nonlinearly saturated states is shown in the figure 6 for RMP equilibrium (panel (*a*)), and for extreme RMP $\times$ 10 equilibrium (panel (*b*)). The color represents the amplitude of electrostatic potential. In both RMP, and RMP $\times$ 10 cases the fluctuation spectrum is peaked at $k_\theta \approx 0.5$ cm^{-1}, and no significant difference is observed in the spectral shape.

The time evolution of self-consistently generated zonal shearing rate magnitude, $\omega_{E\times B} = \partial_r v_{E\times B}$, is shown in the figure 7. Our simulation demonstrates insignificant effect of non-axisymmetry on zonal flow generation. Moreover, we have found that in this localized edge simulation electrostatic turbulence is saturated by resonant detuning, rather than by zonal flow shearing, even though the shearing rate is stronger than the mode growth rate. This conclusion is based on the small difference between heat fluxes observed in self-consistent simulation, and in the simulation where zonal flow is artificially removed. Similar behaviour of reduced turbulence suppression by zonal flow due its fast variation is described in [22].

4. Effect of RMP on kinetic-ballooning mode stability

We have carried out electromagnetic studies by using the same equilibrium profiles as for electrostatic simulations (figure 2), corresponding to the maximum pedestal pressure gradient in the DIII-D shot 158103. However, due to relatively low electron density, the KBM is found to be stable in this case. In order to enhance the KBM instability we have artificially increased the local plasma density used in simulations by roughly a factor of two, while keeping the gradients at the experimental value. As a result β_e has increased well above the KBM stability threshold. This demonstrates that the original profile is close to the KBM threshold, as found in other studies [14].

Based on our previous simulations of KBM in DIII-D pedestal [14], we have focused on the dominant $n = 20$ mode. To address the effect of perturbed magnetic geometry we run simulations with the identical plasma profiles using axisymmetric, RMP, and RMP $\times$ 10 magnetic equilibria.

The poloidal KBM mode structure observed in simulations with RMP and with RMP $\times$ 10 equilibrium are shown in the figure 8, with the color representing the amplitude of the perturbed electrostatic potential. The mode structure looks similar in both RMP, and RMP $\times$ 10 cases, despite the strong distortion of the shapes of magnetic flux surfaces.

The real frequencies and growth rates of the $n = 20$ KBM obtained from linear electromagnetic GTC simulations are shown in the table 2. As we can see, there is no significant effects of RMP perturbation on the stability of KBM, compared to the axisymmetric case. The detectable destabilizing effect can only be observed in the case of 10$\times$ magnified RMP level.

5. Conclusions

In this work we present the results of gyrokinetic simulations addressing the effects of vacuum resonant magnetic perturbation on pressure gradient driven instabilities and transport in a typical DIII-D experiment with applied $n = 2$ RMP. Specifically the analysis focused on the effects of the ideal MHD response to the vacuum resonant RMP calculated by the VMEC code. The ideal MHD response contains the coupling of the external fields to the plasma kink response but excludes resonant field effects in the plasma such as island formation. Three reference equilibria were constructed: axisymmetric (no RMP) equilibrium, $n = 2$ RMP equilibrium, and artificially amplified RMP $\times$ 10 equilibrium. It is found that even in the extreme RMP $\times$ 10 case the turbulent transport is practically unaffected by the ideal MHD kink response magnetic perturbation. Statistical properties of the turbulent spectrum and zonal flow shearing rate are not significantly affected either. Electromagnetic simulations reveal no significant effects of RMP perturbed ideal MHD equilibrium on the stability of the kinetic ballooning mode. Very modest (below 10%) increase of KBM growth rate is observed when 10$\times$ amplified RMP is applied. These results demonstrate that other physics must be controlling the transition in transport responsible for the profile changes leading to ELM suppression. More specifically, the transition to ELM suppression cannot be due to the direct effect of the ideal MHD plasma response on electrostatic or electromagnetic modes. This leads to one of two remaining possibilities: (i) that the ideal MHD response of the plasma affects a different (nonturbulence) transport channel, and/or (ii) that nonideal effects associated with the formation of resonant internal fields play a dominant role in the changes to edge transport leading to profile modification and the ELM suppression.

Acknowledgments

This research used resources of the Oak Ridge Leadership Computing Facility at Oak Ridge National Laboratory (DOE Contract No. DE-AC05-00OR22725), and the National Energy Research Scientific Computing Center (DOE Contract

No. DE-AC02-05CH11231). This work is supported by General Atomics subcontract 4500055243, U.S. DOE theory grant DE-SC0010416 and DE-SC0013804, and by General Atomics collaboration agreement under DOE grant DE-FG03-94ER54271 and by the U.S. DOE grant to the Princeton Plasma Physics Lab., award No. DE-AC02-09CH11466.

References

[1] Evans T.E. *et al* 2006 *Nat. Phys.* **2** 419
[2] Wade M.R. *et al* 2015 *Nucl. Fusion* **55** 023002
[3] Nazikian R. *et al* 2015 *Phys. Rev. Lett.* **114** 105002
[4] McKee G.R. *et al* 2013 *Nucl. Fusion* **53** 113011
[5] Burrell K.H. *et al* 2002 *Plasma Phys. Control. Fusion* **44** A253
[6] Bird T.M. and Hegna C.C. 2014 *Phys. Plasmas* **21** 100702
[7] Ham C.J., Chapman I.T., Kirk A. and Saarelma S. 2014 *Phys. Plasmas* **21** 102501
[8] Leconte M., Diamond P.H. and Xu Y. 2014 *Nucl. Fusion* **54** 013004
[9] Callen J.D., Hegna C.C. and Cole A.J. 2013 *Nucl. Fusion* **53** 113015
[10] Rozhansky V. *et al* 2011 *Nucl. Fusion* **51** 083009
[11] Waltz R.E. and Ferraro N.M. 2015 *Phys. Plasmas* **22** 042507
[12] Paz-Soldan C. *et al* 2015 *Phys. Rev. Lett.* **114** 105001
[13] Hirshman S.P. and Whitson J.C. 1983 *Phys. Fluids* **26** 3553
[14] Holod I., Fulton D. and Lin Z. 2015 *Nucl. Fusion* **55** 093020.
[15] Lin Z., Hahm T.S., Lee W.W., Tang W.M. and White R.B. 1998 *Science* **281** 1835
[16] Lin Z., Nishimura Y., Xiao Y., Holod I., Zhang W.L. and Chen L. 2007 *Plasma Phys. Control. Fusion* **49** B163
[17] Holod I., Zhang W.L., Xiao Y. and Lin Z. 2009 *Phys. Plasmas* **16** 122307
[18] Deng W., Lin Z. and Holod I. 2012 *Nucl. Fusion* **52** 023005
[19] Xiao Y., Holod I., Wang Z.X., Lin Z. and Zhang T.G. 2015 *Phys. Plasmas* **22** 022516
[20] Wingen A. *et al* 2015 *Plasma Phys. Control. Fusion* **57** 104006
[21] Dimits A.M. 2012 *Phys. Plasmas* **19** 022504
[22] Hahm T.S., Beer M.A., Lin Z., Hammett G.W., Lee W.W. and Tang W.M. 1999 *Phys. Plasmas* **6** 922